Resonant bonding driven giant phonon anharmonicity and low thermal conductivity of phosphorene

Guangzhao Qin,[1] Xiaoliang Zhang,[1] Sheng-Ying Yue,[2] Zhenzhen Qin,[3] Huimin Wang,[1] Yang Han,[1] and Ming Hu[1,2,*]

[1]*Institute of Mineral Engineering, Division of Materials Science and Engineering, Faculty of Georesources and Materials Engineering, RWTH Aachen University, Aachen 52064, Germany*

[2]*Aachen Institute for Advanced Study in Computational Engineering Science (AICES), RWTH Aachen University, Aachen 52062, Germany*

[3]*College of Electronic Information and Optical Engineering, Nankai University, Tianjin 300071, China*

(Received 12 August 2016; published 26 October 2016)

Two-dimensional (2D) phosphorene, which possesses fascinating physical and chemical properties distinctively different from other 2D materials, calls for a fundamental understanding of thermal transport properties for its rapidly growing applications in nano- and optoelectronics and thermoelectrics. However, even the basic phonon property, for example, the exact value of the lattice thermal conductivity (κ) of phosphorene reported in the literature, can differ unacceptably by one order of magnitude. More importantly, the fundamental physics underlying its unique properties such as strong phonon anharmonicity and unusual anisotropy remains largely unknown. In this paper, based on the analysis of electronic structure and lattice dynamics from first principles, we report that the giant phonon anharmonicity in phosphorene is associated with the soft transverse optical (TO) phonon modes and arises from the long-range interactions driven by the orbital governed resonant bonding. We also provide a microscopic picture connecting the anisotropic and low κ of phosphorene to the giant directional phonon anharmonicity and long-range interactions, which are further traced back to the asymmetric resonant orbital occupations of electrons and characteristics of the hinge-like structure. The unambiguously low κ of phosphorene obtained consistently by three independent *ab initio* methods confirms the phonon anharmonicity to a large extent and is expected to end the confusing huge deviations in previous studies. This work further pinpoints the necessity of including *van der Waals* interactions to accurately describe the interatomic interactions in phosphorene. We propose in 2D material that resonant bonding leads to low thermal conductivity, despite that it is originally found in three-dimensional (3D) thermoelectric and phase-change materials. Our study offers insights into phonon transport from the view of orbital states, which would be of great significance to the design of emerging phosphorene-based nanodevices.

DOI: 10.1103/PhysRevB.94.165445

I. INTRODUCTION

Phosphorene, the single-layer counterpart of black phosphorus (BP), is a novel elemental two-dimensional (2D) semiconductor with high carrier mobility [1–3] and intrinsic direct band gap [4], which is promising for various applications in nanoelectronics complementary to existing 2D semiconductors, such as graphene, silicene, germanene, and transition-metal dichalcogenides (TMDCs) [1–15]. Tremendous amount of theoretical and experimental work have already been dedicated to exploring the fantastic applications of phosphorene as nanoelectronic devices, such as field-effect transistors, phototransistors, and thermoelectrics [1–3,11–15]. Since heat transfer plays a critical role in all these applications, such as efficient heat dissipation for nano- and optoelectronic devices and minimized thermal conductivity for thermoelectrics, the potentially valuable applications involving phosphorene demand fundamental study of its thermal transport (mainly phonons) properties.

To date, there are some experimental measurements of the thermal conductivity of bulk BP [16] and phosphorene films with different thickness [17–19]. The thermal conductivity of phosphorene was investigated theoretically by several independent groups using various methods, such as analytical estimation [11,20], classical molecular dynamics (MD) simulation with optimized Stillinger-Weber potential [21–23], single relaxation time approximation (RTA) [16,24–26] and the iterative method for solving the Boltzmann transport equation (BTE) [16,25]. However, the results obtained differ from each other unacceptably by even one order of magnitude. For example, the thermal conductivity of phosphorene along the zigzag direction ranges from 30 to 152.7 $\mathrm{W\,m^{-1}\,K^{-1}}$, while thermal conductivity along the armchair direction varies from 9.9 to 63.9 $\mathrm{W\,m^{-1}\,K^{-1}}$ [11,21–23]. Therefore, it is necessary to perform a systematic study to precisely predict the thermal conductivity of phosphorene, which would be of great significance to the design of efficient phosphorene-based nanoelectronics. Moreover, although the common knowledge of phosphorene possessing strong anisotropy and unusual phonon anharmonicity has been established [25–27], the fundamental origin underneath, especially from the point of view of electronic structure and interatomic bonding, still remains largely unclear.

In this paper, we provide a coherent microscopic picture connecting the anisotropic and low thermal conductivity of phosphorene to giant directional phonon anharmonicity and long-range interactions, which are traced back to the orbital governed resonant bonding and characteristics of the intrinsic hinge-like structure at the end. The anisotropic and low thermal conductivity of phosphorene is confirmed consistently by employing three independent *ab initio* methods. This study yields unambiguously low thermal conductivity of phosphorene and undoubtedly elucidates the governing mechanism, which is critical to promote the innovative development of phosphorene-based nanoelectronics.

*hum@ghi.rwth-aachen.de

II. METHODOLOGY

A. First-principles calculations

All the first-principles calculations are performed based on density functional theory (DFT) using the projector augmented wave (PAW) method [28] as implemented in the Vienna *ab initio* simulation package (VASP) [29]. The Perdew-Burke-Ernzerhof (PBE) [30] of the generalized gradient approximation (GGA) is chosen as the exchange-correlation functional and *van der Waals* (vdW) interactions are taken into account at the vdW–density functional (vdW-DF) level with optB88 used as the exchange functional [31]. The kinetic energy cutoff of wave functions is set as 700 eV and a Monkhorst-Pack [32] k-mesh of $15 \times 11 \times 1$ is used to sample the Brillouin zone (BZ) with energy convergence threshold set as 1×10^{-8} eV. A large vacuum spacing of at least 15 Å along the *out-of-plane* direction is used to hinder the interactions between the layer and the mirrored layer arising from the employed periodic boundary conditions. Both cell shape and volume are fully optimized and all atoms are allowed to relax until the maximal Hellmann-Feynman force acting on each atom is no larger than 1×10^{-8} eV/Å.

B. Finite displacement difference (FDD) method

Based on the optimized structure and the convergence test of phonon dispersions, a $5 \times 5 \times 1$ supercell containing 100 atoms is constructed [26]. In the supercell calculations for obtaining harmonic (second-order) interatomic force constants (IFCs) and anharmonic (third-order) IFCs, only the Γ point in the reciprocal space is used for the purpose of fast computing speed [33]. The harmonic IFCs are obtained using the real-space FDD method, in which the force constants $C_{i\alpha;j\beta}$ can be obtained from the force caused by atomic displacement:

$$C_{i\alpha;j\beta} = -\frac{F_{i\alpha}}{\Delta_{j\beta}}, \tag{1}$$

where $F_{i\alpha}$ is the force along the α direction acting on atom i resulted from the displacement along the β direction of atom j ($\Delta_{j\beta}$). The displacement amplitude of an atom along the $\pm x$, $\pm y$, and $\pm z$ directions is 0.01 Å. The space group symmetry properties are used to reduce the computing cost and numerical noise of the force constants, and they can also greatly simplify the determination of the dynamical matrix that is constructed based on the IFCs. The frequencies and eigenvectors forming the phonon dispersion are obtained by diagonalizing the dynamical matrix using the PHONOPY [34] package. For calculating the anharmonic IFCs, the same $5 \times 5 \times 1$ supercell and similar FDD method are employed. The translational and rotational invariances of IFCs are enforced using the Lagrange multiplier method [35,36]. A cutoff radius (r_{cutoff}) is introduced to disregard the interactions between atoms with distance larger than a certain value for practical purposes. In principle, the r_{cutoff} should exceed the range of physically relevant anharmonic interactions to get satisfactory results [36,37], which should be carefully tested with respect to the convergence of κ. Based on the κ vs r_{cutoff} as shown in Fig. 4(a), interactions up to the 20th nearest neighbors were taken into account, which corresponds to a cutoff distance of 7.85 Å. Such a choice of cutoff distance gives the converged κ of phosphorene.

C. Anharmonic lattice dynamics (ALD)

Based on the harmonic and anharmonic IFCs, the ALD method is employed to calculate the phonon lifetime by constructing the scattering matrix and to further get κ by solving the linearized BTE for phonons:

$$\kappa_\alpha = \sum_{\vec{q}p} C_{\text{V}} v_\alpha(\vec{q},p)^2 \tau(\vec{q},p), \tag{2}$$

where C_{V} is the phonon volumetric specific heat, and $\vec{v}_\alpha(\vec{q},p)$ is the $\alpha(=x,y,z)$ component of the group velocity of the phonon mode with wave vector $\vec{q}$ and polarization p. The dielectric tensor and Born effective charges are obtained based on the density functional perturbation theory (DFPT), which is added to the dynamical matrix as a correction for taking into account long-range electrostatic interactions. The thickness of phosphorene is chosen as 5.36 Å, which is half the length of the lattice constant along the *out-of-plane* direction of the layered bulk counterpart containing two layers in the conventional cell [12,38]. All the possible three-phonon scattering events are determined based on the phonon dispersion by conserving both energy and crystal momentum:

$$\omega_j(\vec{q}) \pm \omega_{j'}(\vec{q'}) = \omega_{j''}(\vec{q''}), \quad \vec{q} \pm \vec{q'} = \vec{q''} + \vec{K}. \tag{3}$$

The normal process corresponds to $\vec{K} = 0$, while the umklapp process corresponds to $\vec{K} \neq 0$. The phonon lifetime τ_λ (where λ is the index of the phonon mode comprising both p and $\vec{q}$) used within the RTA can be computed as

$$\frac{1}{\tau_\lambda^0} = \frac{1}{N}\left(\sum_{\lambda'\lambda''}^{+} \Gamma^{+}_{\lambda\lambda'\lambda''} + \sum_{\lambda'\lambda''}^{-} \frac{1}{2}\Gamma^{-}_{\lambda\lambda'\lambda''} + \sum_{\lambda'} \Gamma_{\lambda\lambda'}\right), \tag{4}$$

where $N = N_1 \times N_2 \times N_3$ is the number of discrete $\vec{q}$ sampling in the BZ, $\Gamma^{+}_{\lambda\lambda'\lambda''}$ and $\Gamma^{-}_{\lambda\lambda'\lambda''}$ are three-phonon scattering rates corresponding to absorption and emission processes of phonons, respectively [39–42], and $\Gamma_{\lambda\lambda'}$ is the scattering possibility resulted from the disorder of isotopic impurity [43,44]. The lattice thermal conductivity can also be obtained by iteratively solving the phonon BTE [36,45]. In principle, the iterative procedure has a large impact when the normal process plays a significant role in the phonon-phonon scattering [40], where the RTA treating the normal process to be resistive will underestimate the thermal conductivity a lot (see Sec. 2 of the Supplemental Material [46]). If the iteration stops at the first step, the procedure is equivalent to the solution of the RTA.

D. Phonon spectral energy density (SED)

To obtain the phonon lifetime, we also carried out phonon SED analysis [47–51]. The phonon normal modes and the SED can be calculated by

$$\dot{Q}(\vec{q},p,t) = \sum_{jl} \sqrt{\frac{m_j}{N}}\, \vec{v}_{jl}(t) \cdot \vec{e}^{\,*}_j(\vec{q},p) \exp(-i\vec{q}\cdot\vec{r}_l),$$

$$\Phi(\vec{q},p,\omega) = \left| \int \dot{Q}(\vec{q},p,t) \exp(-i\omega t) dt \right|^2, \tag{5}$$

where m_j is mass of the jth atom, N is the number of unit cells, $\vec{v}_{jl}$ is the velocity of the jth atom located inside the lth unit cell ($\vec{r}_l$), and $\vec{e}_j(\vec{q},p)$ is the eigenvector of the phonon mode.

The atomic velocities are obtained from equilibrium *ab initio* molecular dynamics (EAIMD) simulations in the NVE (constant energy without thermostat) ensemble as implemented in VASP [29]. The phonon lifetime can be obtained by fitting the SED peak [$\Phi(\vec{q},p,\omega)$] with the Lorentzian function (see Sec. 3 of the Supplemental Material [46]):

$$\Phi(\vec{q},p,\omega) = \frac{I}{1+\left(\frac{\omega-\omega_0}{\Gamma}\right)^2}, \tag{6}$$

where I is the peak magnitude, ω_0 is the frequency at the peak center, and Γ is the half width at half maximum. Finally, the phonon lifetime is defined as $\tau = 1/(2\Gamma)$. Four different $N \times N \times 1$ ($N = 5,6,7,8$) supercells are constructed to run EAIMD simulations for generating atomic velocities. For each supercell we perform five independent runs to obtain the average SED. All the simulation temperatures are around 300 K. Once the phonon lifetime is obtained by fitting the SED peak, the thermal conductivity can be calculated using Eq. (2).

E. Non-equilibrium *ab initio* molecular dynamics (NEAIMD) simulations

The NEAIMD simulations are performed to calculate the thermal conductivity of phosphorene by Fourier's law:

$$\kappa_{\text{NEAIMD}} = -\frac{J}{\nabla T}, \tag{7}$$

where J is the averaged heat flux along the longitudinal direction and ∇T is the temperature gradient determined from the linear fitting of the time-averaged temperature profile along the same direction. Considering the much larger mean free path (MFP) along the zigzag direction (9.6 nm) than that along the armchair direction (5.9 nm) and the limited maximal simulation size in NEAIMD, we only performed simulations with the heat flux applied along the armchair direction (see Sec. 4 in the Supplemental Material [46]). The NEAIMD simulations are performed for seven different system lengths ranging from 2.3 to 9.2 nm using a modified version of the VASP code [29,52,53], in which the atomic heat flux is realized by the Müller-Plathe algorithm [54]. With a time step of 1 fs, the kinetic energy of selected atoms in the heat source and heat sink are exchanged every 50 steps. Such an action will impose a steady heat flux and a corresponding temperature gradient after running a long enough simulation time. The heat flux is determined by fitting the accumulative exchanged energy vs simulation time. By linearly fitting the time-averaged temperature profile of each system, the ∇T can be obtained to calculate the thermal conductivity.

F. Length dependence and phonon boundary scattering

In order to address the length-dependent phonon transport properties, the phonon boundary scattering due to the finite length of the sample should be considered, which can be estimated based on ALD/BTE by the standard equation [55–57]:

$$\frac{1}{\tau^B(\vec{q},p)} = \frac{1-p}{1+p}\frac{|v_\alpha(\vec{q},p)|}{L}, \tag{8}$$

where p is the specularity parameter, which means the fraction of specularly scattered phonons depending on the roughness of the edge, $\vec{v}_\alpha(\vec{q},p)$ is the $\alpha(=x,y,z)$ component of the phonon group velocity along the heat transport direction, and L is the system size, usually ranging from nanometers to micrometers. The p parameter ranges from zero for a completely rough edge to one for a perfectly smooth edge. The temperature gradient is assumed to be along the direction of the finite sample length. Finally, the scattering rate of each mode is calculated by the Matthiessen rule:

$$\frac{1}{\tau(\vec{q},p)} = \frac{1}{\tau^{\text{anh}}(\vec{q},p)} + \frac{1}{\tau^{\text{iso}}(\vec{q},p)} + \frac{1}{\tau^{\text{B}}(\vec{q},p)}, \tag{9}$$

where $1/\tau^{\text{anh}}$ is the intrinsic anharmonic scattering rates due to phonon-phonon interactions and $1/\tau^{\text{iso}}$ is the scattering rate due to isotopic impurity.

III. RESULTS

A. Soft phonon modes and giant anharmonicity

Phosphorene possesses a puckered (hinge-like) structure along the armchair direction [Figs. 1(a) and 1(b)], which is distinctly different from the planar graphene and buckled silicene structures [12,58–62]. The hinge-like orthorhombic structure generally introduces anisotropic properties, such as softer stiffness along the armchair direction than the zigzag direction, which can be quantified by Young's modulus, and leads to much larger lattice constants along the armchair direction (4.58 Å) than along the zigzag direction (3.32 Å) [6,63]. Based on the optimized structure, the phonon dispersion and the corresponding density of states (DOS) are calculated, as shown in Fig. 1(c), which is consistent with previous studies [8,11]. It is clearly seen that there is a gap between 8 and 10 THz, which separates the phonon branches into two regions with each region containing six branches. The region below the gap shows obvious anisotropy along Γ-X and Γ-Y paths, which is analogous to other 2D materials with similar hinge-like structure [64].

From the phonon dispersion, we notice that there exist soft phonon modes, i.e., TO_z, with frequency decreasing near the BZ center (Γ point), as highlighted in red in Fig. 1(c). The behavior of phonon softening can be more clearly seen in the 3D phonon dispersions [Figs. 1(d) and 1(e)]. Previous studies have demonstrated that TO phonon softening principally induces strong phonon anharmonicity [27,65], which can be quantified by the Grüneisen parameter (γ). As plotted in Fig. 2(d), it is clearly shown that the soft TO_z modes possess strong anharmonicity, while the LO_y and TO_x modes do not. The TO_z correlates strongly with the distortion of P atoms along the *out-of-plane* direction (see Sec. 5 in the Supplemental Material [46]). To have an explicit look at the anharmonicity associated with the soft TO_z modes, the potential energy well (potential energy changes due to the atomic displacement) along the *out-of-plane* direction felt by the P atom is plotted in Fig. 2(c). Note that we only move one P atom because the four P atoms in the unit cell are equivalent due to structural symmetry [6]. For comparison, the potential energy wells along the two *in-plane* (zigzag and armchair) directions are also plotted [Figs. 2(a) and 2(b)]. The potential well is asymmetric with respect to the positive and negative atomic displacements, indicating the asymmetry in the ability of an atom to vibrate around its equilibrium

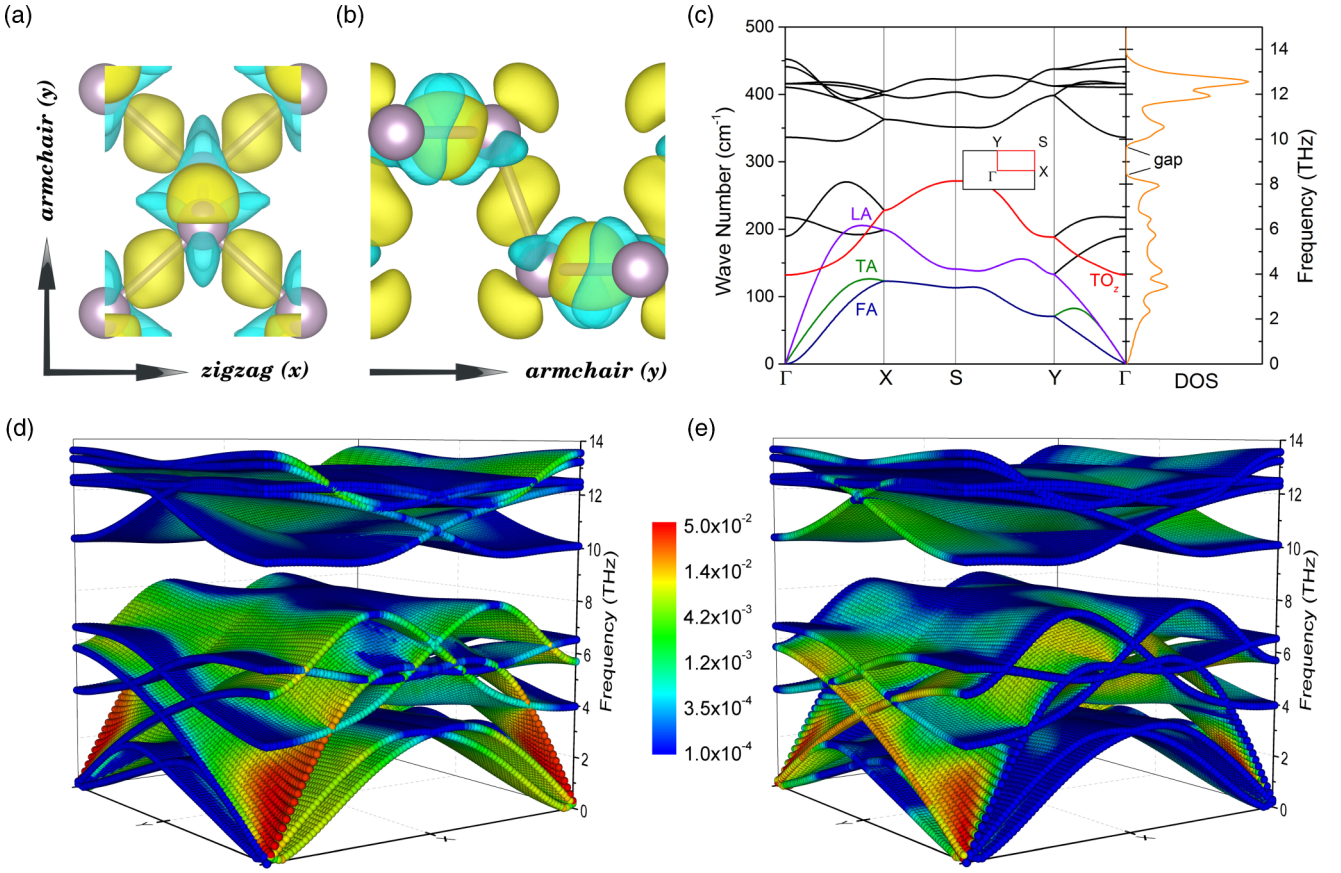

FIG. 1. Charge density difference (total density minus the sum of atomic densities) and three-dimensional (3D) phonon dispersion of phosphorene. (a) Top view and (b) side view of the change density difference (yellow, positive; cyan, negative) with zigzag (x) and armchair (y) directions indicated (isosurface level, 0.007). (c) Phonon dispersion and density of states (DOS) of phosphorene. The soft *out-of-plane* transverse optical (TO_z) phonon branch and the three acoustic phonon branches are labeled and plotted in different colors. Inset: The Brillouin zone (BZ) with high-symmetry k-points indicated. The 3D phonon dispersion in the whole BZ with color indicating the phonon mode contribution (percentage) to the total thermal conductivity along (d) zigzag and (e) armchair directions. Thermal conductivity and its anisotropy are mainly contributed (85%) by phonon modes below the gap (see Sec. 1 of the Supplemental Material [46]).

position and the nonlinear dependence of restoring forces on atomic displacement amplitudes, which is the direct evidence of the anharmonicity [66,67]. By polynomial fitting to the potential energy wells, the fitted parameter for the cubic term is zero for the x direction, -843.4 meV/Å^3 for the y direction, and 1243.2 meV/Å^3 for the z direction. The largest absolute value of the cubic term for the z direction indicates that the potential well deviates from the parabolic (harmonic) behavior most severely when the atomic displacement is along the *out-of-plane* direction, which confirms the strongest phonon anharmonicity associated with TO_z. It is interesting to note that the potential well is harmonic when the reference P atom moves along the zigzag direction, which is directly due to the structural symmetry.

The harmonicity or anharmonicity of the potential wells and the symmetric or asymmetric behavior can be traced back to the response of the electronic structure to geometric structure distortions. The calculated orbital projected density of states (pDOS) of electrons (s, p_x, p_y, and p_z) are plotted in Fig. 2(h). The bonding states near the valence-band maximum (VBM) are dominated by the p_z orbital, which forms a broad band (~6 eV) hybridized with the p_x and p_y orbitals and mediated by the s orbital. The s orbital is mainly confined 9 eV below the VBM, showing weak hybridization with the p_x, p_y, and p_z orbitals (see Sec. 6 of the Supplemental Material [46]). The pDOS changes with respect to the positive and negative displacements of the reference P atom along different directions, which is the electronic origin of the symmetric (harmonicity) or asymmetric (anharmonicity) behavior of the potential well. For example, the pDOS changes in a symmetric way [Figs. 2(e) and 2(i)] when the P atom distorts along the zigzag ($\pm x$) direction, while it changes in an asymmetric way for the armchair ($\pm y$) [Figs. 2(f) and 2(j)] and *out-of-plane* ($\pm z$) [Figs. 2(g) and 2(k)] directions. All these behaviors are consistent with the potential well as shown in Figs. 2(a)–2(c). More specifically, The pDOS almost does not change with the distortion of atoms along the zigzag direction, especially near the VBM, where the bonding states keep dominated by the p_z orbital [Figs. 2(e) and 2(i)]. The potential well is symmetric for atomic displacement along the zigzag direction due to the consistency of the bonding states near the VBM, whereas for atomic displacement along the armchair or *out-of-plane* direction, the bonding states near the VBM as reflected by the pDOS change from the p_z orbital to the p_x or p_y orbital [Figs. 2(f) and 2(j)], or the hybridization of the p_z orbital with the p_x and p_y orbitals becomes stronger [Figs. 2(g) and 2(k)],

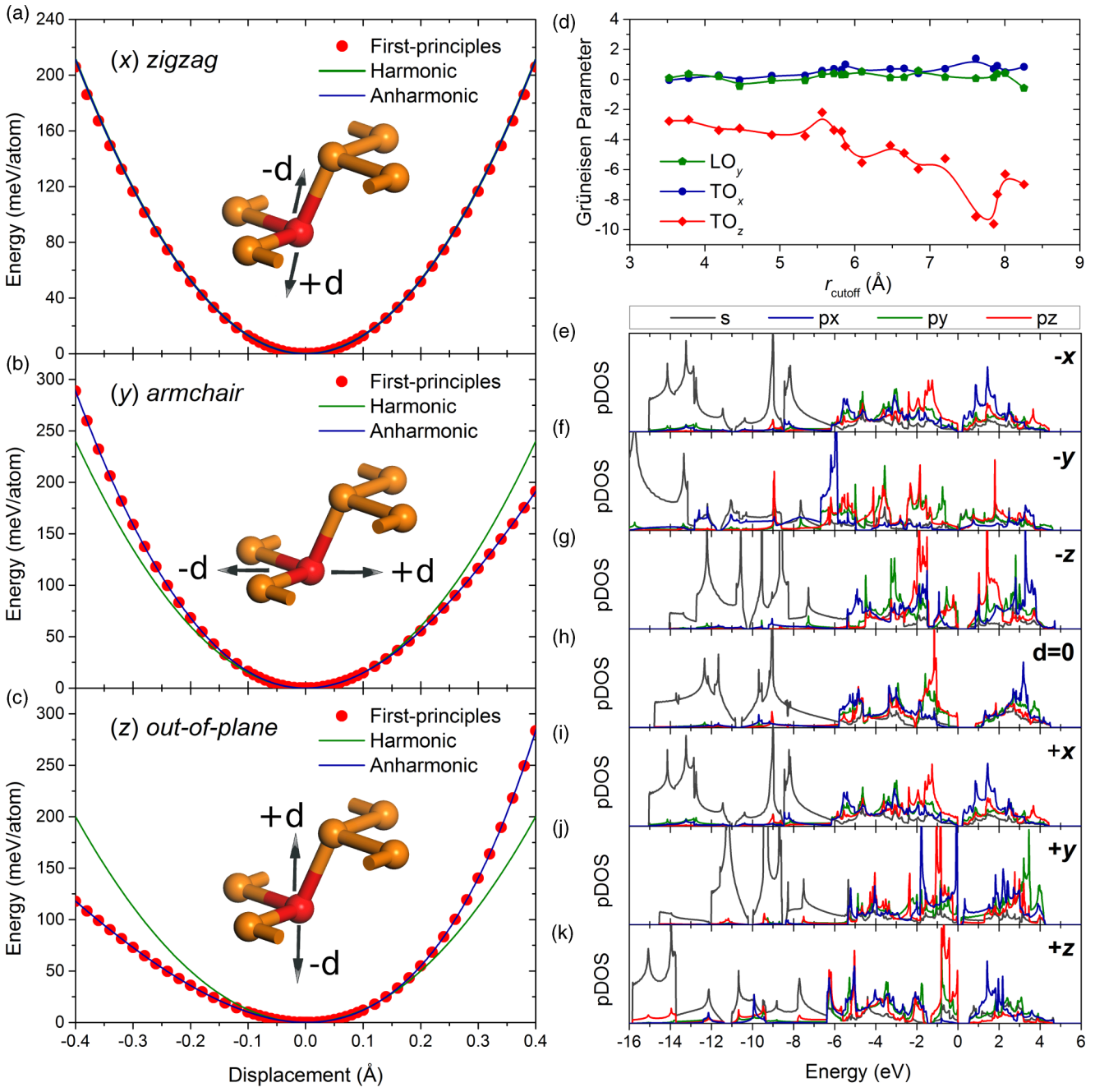

FIG. 2. Analysis of phonon anharmonicity in phosphorene by first-principles calculations. (a–c) Potential energy change per atom (together with harmonic and anharmonic fitting) with respect to displacement of the P atom along the zigzag (x), armchair (y), and *out-of-plane* (z) directions. The anharmonic fitting is performed with the polynomial function up to the cubic term. Inset: Schematic of atomic displacement. (d) Convergence of Grüneisen parameters (γ) with respect to r_{cutoff} for zone-center (Γ) optical phonon modes polarized along the x, y, and z directions, respectively. (e–k) The orbital projected density of states (pDOS) of electrons (s, p_x, p_y, and p_z) for structures at equilibrium [$d = 0$, (h)] and modulated by negative (e–g) and positive (i–k) displacements of the P atom along the x, y, and z directions.

leading to the anharmonicity revealed by the potential well. Therefore, the fundamental understanding of the phonon anharmonicity is achieved from the microscopic point of view of orbital states based on the analysis of the electronic structure.

The change of the bonding states near the VBM due to the atomic displacement can be further traced back to the distortion of bond length. First, to make clear the characteristics of bonding and its relationship with orbitals, we plot the highest occupied molecular orbital (HOMO) corresponding to the VBM [Fig. 3(a)], which is a typical σ bond mainly contributed by the p_z orbital (see Sec. 6 of the Supplemental Material [46]). It is shown that the overlap of the p_z orbital among P atoms forms the vertical bond along the *out-of-plane* direction. If the P atom displaces along the $+z$ (*out-of-plane*) direction as shown in the inset of Fig. 2(c), the vertical bond is shortened, causing stronger overlap of the p_z orbital among P atoms [66], which is reflected by the right shift to the VBM of the p_z-orbital peak [Fig. 2(k)]. On the contrary, the vertical bond

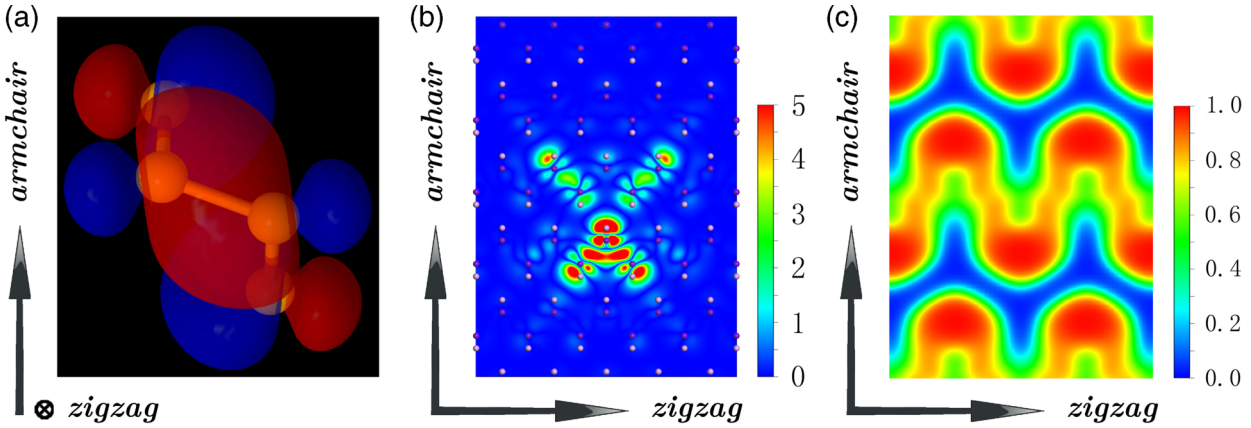

FIG. 3. Characteristics of bonding and behavior of electrons in phosphorene. (a) Side view of the highest occupied molecular orbital (HOMO) (p-type σ bond; blue, positive; red, negative), corresponding to the valence-band maximum (isosurface level, 0.03). (b) Absolute charge density change due to the displacement (0.02 Å along the z direction) of the central nether P atom within a $5 \times 5 \times 1$ supercell, showing long-range interactions along the [110] direction. The plot is top view and atoms are marked on site (upside atoms are in dark purple). The unit is 10^{-5} e Å^{-3}. (c) Top view of electron localization function (ELF) within a $2 \times 2 \times 1$ supercell.

will be elongated by the displacement of the P atom along the $-z$ direction, causing weaker overlap of the p_z orbital among P atoms, which is reflected by the left shift away from the VBM of the p_z-orbital peak [Fig. 2(g)]. The changes of bonding states near the VBM with respect to the *in-plane* atomic displacements can also be analyzed in a similar way (see Sec. 7 of the Supplemental Material [46]).

B. Resonant bonding and long-range interactions

From the calculated pDOS of electrons, we know that the bonding states near the VBM are dominated by the p_z orbital hybridized with the p_x and p_y orbitals, and the s orbital is confined largely below the VBM, exhibiting weak hybridization with the p_x, p_y, and p_z orbitals [Fig. 2(h)]. The weak sp hybridization is typically a premonitor for the formation of the resonant bonding [68]. The two s electrons forming a lone pair are localized around P atom [Figs. 1(a) and 1(b)], while the p electrons are highly delocalized due to the resonant bonding (see Sec. 8 in the Supplemental Material [46]) [68,69]. In fact, the hinge-like structure of phosphorene can be regarded as a deformed rocksalt structure, where, due to the unsaturated covalent bonding of p electrons, the formed bonding is a resonance or hybridization among different electronic configurations of p-electron occupations (see Sec. 7 of the Supplemental Material [46]) [69]. Owing to the structural distortion of the hinge-like structure of phosphorene from the perfect rocksalt structure, the resonant bonding in phosphorene exists in a weakened form as compared with that in regular rocksalt structures [68,69]. However, it still has a significant impact on long-range interactions and phonon anharmonicity, and finally affects the phonon transport, as we see shortly.

Based on the analysis of the IFCs, the normalized absolute trace of the IFC tensors [68] shows strong long-range interactions at the separation distance of approximate 6 Å (corresponding to the 13th nearest neighbors), which are stronger than the interactions of much nearer neighbors, such as the second- or third-nearest neighbors (see Sec. 9 of the Supplemental Material [46]). This is proved by the perturbation of the charge density distribution due to the displacement of the central nether P atom within a $5 \times 5 \times 1$ supercell [Fig. 3(b)]. It shows that the disturbance along the [110] direction can reach as far as the 13th nearest neighbors (∼6 Å), corresponding to the fourth nearest neighbors in the rocksalt structure [68]. The significant long-range IFC components result from the long-range charge density perturbation induced by atomic displacement [70], which are particularly extended along the [110] direction, corresponding to the collinear bonding direction of the resonant bonding in the hinge-like structure of phosphorene. The long-range perturbations of the charge density distribution are the most significant when the displacement is along the *out-of-plane* direction as compared with the *in-plane* directions, which is consistent with the giant anharmonicity associated with the soft TO_z phonon modes (see Sec. 10 of the Supplemental Material [46]). In addition to the identified long-range interactions due to the resonant bonding, the charge density perturbation induced by atomic displacement also confirms that the $5 \times 5 \times 1$ supercell is sufficiently large for calculating the harmonic and anharmonic IFCs that are needed for the following κ calculation. From the microscopic view of the electronic structure and the lattice dynamics of phosphorene, we provide a picture of the link of resonant bonding from the weak sp hybridization, the giant phonon anharmonicity due to the long-range interactions, and the resulted soft TO phonon modes, based on which one intuitively expects low κ of phosphorene.

C. Thermal conductivity from three independent *ab initio* methods

To obtain the exact κ of phosphorene, three independent *ab initio* methods are employed:

(1) ALD/BTE: Solve the phonon BTE with phonon lifetime determined by the ALD method with IFCs evaluated from *ab initio* calculations [29,45].

(2) SED/EAIMD: Obtain the phonon lifetime straightforwardly using the SED technique with the trajectory of atomic velocities obtained from EAIMD simulations [48,71].

(3) NEAIMD: Perform direct NEAIMD simulations to calculate the thermal conductivity by Fourier's law [29,52].

The results are consistent with each other as presented below in sequence.

For calculating the anharmonic IFCs, the cutoff radius (r_{cutoff}) is chosen as 7.85 Å based on the convergence test of κ vs r_{cutoff} [Fig. 4(a)], which means that the interactions are taken into account up to the 20th nearest neighbors. The large r_{cutoff} is completely due to the resonant bonding induced long-range interactions [Fig. 3(b)] as discussed above. Such a choice of r_{cutoff} finally yields converged κ of 15.33 W m^{-1} K^{-1} (zigzag) and 4.59 W m^{-1} K^{-1} (armchair) for phosphorene at 300 K. As shown in the inset of Fig. 4(a), the κ along both zigzag and armchair directions show size (Q-grid) independence, which is distinctly different from the result from Zhu *et al.* [24], where they claim that there exists a coexistence of size-dependent and size-independent thermal conductivities along the zigzag and armchair directions, respectively. The discrepancy lies in the far from large enough cutoff distance (4.4 Å) used in their calculations. Actually, using the same cutoff distance we also found the similar phenomenon (see Sec. 11 of the Supplemental Material [46]). The size-dependent κ in the case of small r_{cutoff} is primarily due to the lifetime of acoustic phonon modes that quickly blows up when approaching the Γ point of the BZ [72]. The lifetime of low-frequency acoustic phonon modes will be suppressed when long-range interactions (∼6 Å) are involved. The so-called coexistence of size-dependent and size-independent behavior of κ disappears when the r_{cutoff} is large enough exceeding the range of physically relevant anharmonic interactions.

Besides the ALD/BTE calculations presented above, the mode-level phonon lifetime can also be obtained in a straightforward way by analyzing the atomic trajectories (velocities in this work) in a crystalline lattice using the phonon SED technique [48,51,71]. Once the phonon lifetime is obtained by the SED technique (see Sec. 3 of the Supplemental Material [46]), the κ can be calculated using Eq. (2). By linearly fitting $1/\kappa$ with respect to the inverse of supercell size ($1/N$) [Fig. 4(b)], the converged κ of phosphorene at 300 K is obtained to be 13.46 W m^{-1} K^{-1} (zigzag) and 5.46 W m^{-1} K^{-1} (armchair), which agrees perfectly with the results from ALD/BTE method. It is interesting to note that κ decreases with larger simulation domain, which is different from the common trend in equilibrium molecular dynamics (EMD) simulations, where κ usually increases with size of simulation domain [60]. The phonon lifetime from the SED/EAIMD method scaled by $\kappa_{\text{converged}}/\kappa$ is plotted in Fig. 4(d) together with the results from the ALD/BTE method, and they agree well with each other. It is worth pointing out that for the ALD/BTE method the lifetime of acoustic phonon modes near the Γ point of the BZ (corresponding to low-frequency phonon modes) remains limited, which is different from the cases with a small r_{cutoff}, where, due to the insufficient involvement of the physically relevant anharmonic interactions, the lifetime of acoustic phonon modes approaching the Γ point blows up, resulting in the size-dependent behavior of κ (see Sec. 11 of the Supplemental Material [46]). This also suggests that the sufficiently large interaction cutoff distance is required to get converged and stable κ in the case of phosphorene.

To address the size effect on the phonon transport properties, the phonon boundary scattering due to finite size is considered by a fully diffusive scattering at the boundary based on the ALD/BTE calculations. The κ as a function of system size (L) is plotted in Fig. 4(c). When the size is up to 1×10^4 nm, the κ of phosphorene converges to the value of an infinitely long system. The κ decreases with size decreasing, and the κ along the zigzag direction has a steeper decrease than that along the armchair direction, which results from its larger MFP. Consequently, the anisotropy of κ becomes weak at short length. We also performed direct NEAIMD simulations with heat flux applied along the armchair direction to calculate the κ of phosphorene (see Sec. 4 of the Supplemental Material [46]). As length becomes larger, more long-wave phonons are available for contributing to the overall thermal transport, leading to the increase of κ with system length. It should be noted that the maximum length as simulated in NEAIMD is about 10 nm, which is larger than the MFP along the armchair direction (5.9 nm from the ALD/BTE method). Therefore, the phonon transport along the armchair direction in phosphorene can easily enter the diffusive regime, even if the simulated system is not too large. The size-dependent κ obtained by NEAIMD agrees well with that estimated by the *ab initio* ALD/BTE method with boundary scattering considered [Fig. 4(c)]. The slight mismatch for the length around 2–3 nm might be due to the inaccuracy of the Matthiessen rule for including the boundary scattering under the assumption of diffusive phonon transport for ALD/BTE at such short length [73].

D. Comparison of the thermal conductivity

There have been lots of studies focusing on the κ of phosphorene (films) from both experiments and theoretical calculations. Due to the difficulty of directly synthesizing monolayer phosphorene [74], experimental results of κ are only available for bulk BP and phosphorene films with thickness ranging from ∼10 to ∼550 nm [16–19]. As for the κ of phosphorene, there are only results from theoretical calculations with different methods [11,16,20–26]. All these results are collected in Fig. 4(e) together with the results from this work obtained using ALD/BTE and SED/EAIMD methods. It is clearly seen that the κ of phosphorene films starts from a high level of bulk BP and decreases with thickness decreasing. Our converged κ of phosphorene is lower than that for phosphorene films with minimum thickness of 9.5 nm. A detailed thickness dependence study of κ of few-layer phosphorene from *ab initio* calculations is currently under way and results will be reported separately. Note that from previous work by Zhang *et al.* based on classical MD, the thermal conductivity of few-layer phosphorene stays consistent until the thickness up to about 4 nm (seven layers) [23], which is quite different from the cases of graphene and MoS_2 [75,76]. The reason for this unusual behavior possibly comes from the much stronger interactions due to the interlayer wave-function overlap [6,74] rather than *van der Waals* interactions. The latter are generally regarded to play a primary role in mediating the interlayer interactions in few-layer graphene and MoS_2.

As for the κ of phosphorene, there have been lots of theoretical studies using various methods, such as analytical estimations [11,20], classical MD simulation with optimized Stillinger-Weber potential [21–23], RTA [16,24–26] and the iterative method based on ALD/BTE [16,25]. However, the

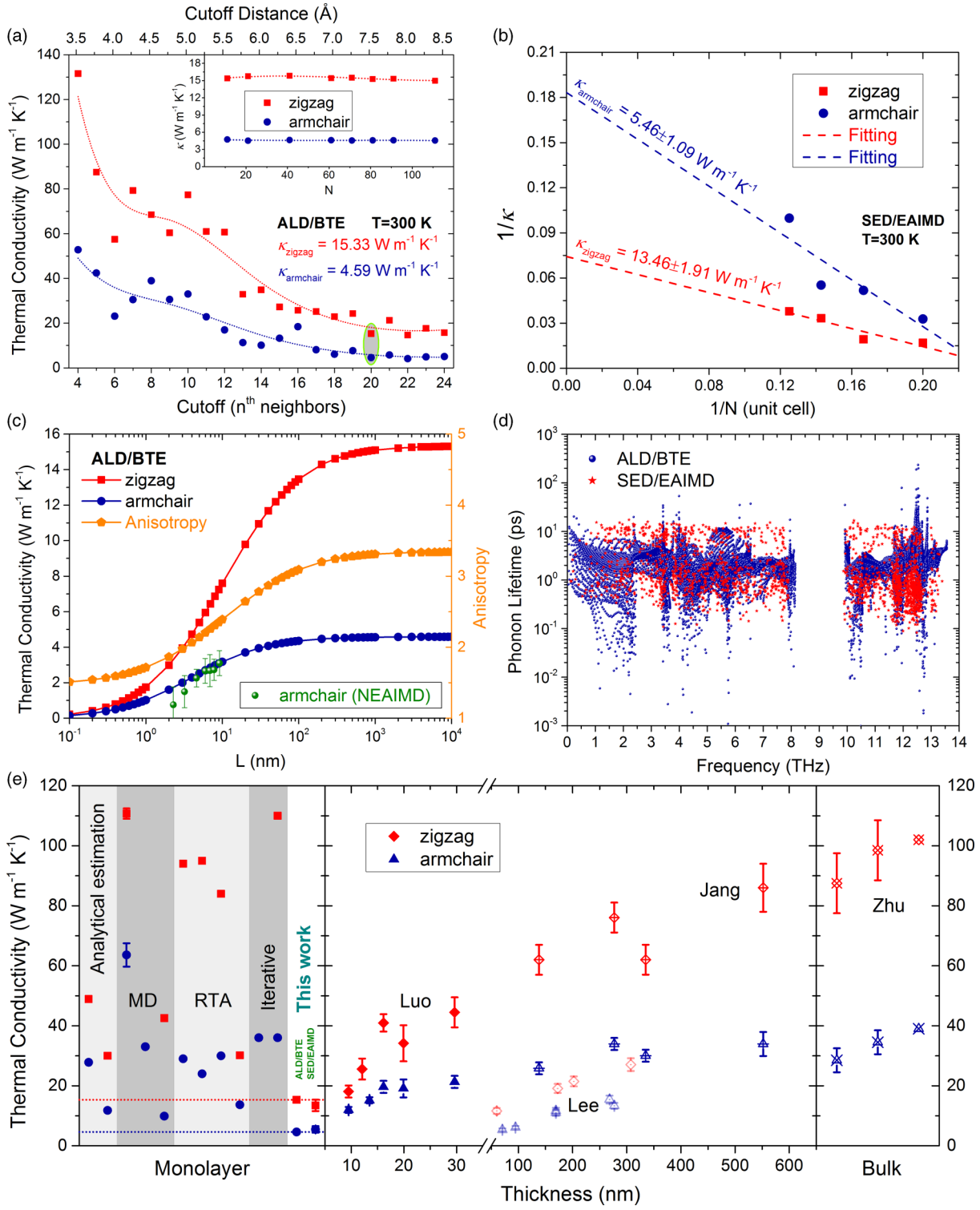

FIG. 4. Phonon transport properties of phosphorene calculated by three independent *ab initio* methods. (a) Lattice thermal conductivity (κ) of phosphorene at 300 K vs the interaction cutoff distance obtained by solving the phonon BTE based on the ALD method. Inset: κ vs Q-grid ($N \times N$). The green (gray) ellipse indicates the cutoff distance that is finally chosen for the reported κ values. (b) Extrapolated κ by linearly fitting the thermal conductivity obtained from SED/EAIMD method with respect to system size. The error of the converged κ is estimated by the standard error in the linear fitting. (c) κ and the anisotropy at 300 K as a function of system size. The anisotropy is defined as $\kappa_{\text{zigzag}}/\kappa_{\text{armchair}}$. The κ along the armchair direction calculated by NEAIMD is plotted for comparison. The error bar is determined based on the calculation of the temperature gradient (∇T) and heat flux (J). (d) The comparison of mode level phonon lifetime between ALD/BTE and SED/EAIMD methods. (e) The comparison of κ from our calculation with experiments and other reported results. Left: κ of phosphorene from different methods by others and the current work [11,16,20–26]. Middle: Experimental κ values of phosphorene films with different thickness [17–19]. Right: κ of bulk BP from both experiment (with error bar) and theoretical calculation [16].

previous results differ largely with each other by almost one order of magnitude [11,21–23]. The huge deviation is due to different calculation methods and computational parameters used. For example, Jain *et al.* calculated κ using the same iterative method based on the ALD/BTE technique as employed in this work, and they also performed the convergence test with respect to the interaction cutoff [25]. However, κ vs the interactions cutoff distance, as calculated in their work, does not show a convincing convergence trend, and the values of κ are quite large. In contrast, the convergence test performed in this work does show a distinct exponential-like decrease trend [Fig. 4(a)] towards the converged low κ of phosphorene. The discrepancy probably originates from two aspects: (1) The scalar relativistic pseudopotential used in their work does not include the *van der Waals* interactions, which have been previously proved to have a significant effect on the properties of bulk BP and phosphorene [6,74]. We performed an additional test by comparing the atomic structure, phonon dispersion, and thermal conductivity with and without *van der Waals* interactions (see Sec. 12 of the Supplemental Material [46]). It turns out that excluding *van der Waals* interactions breaks the formation of resonant bonding by affecting lattice constants and the distance between P atoms, leading to much higher κ (zigzag, 129.47 $\mathrm{Wm^{-1}K^{-1}}$; armchair, 23.04 $\mathrm{Wm^{-1}K^{-1}}$) for the same interaction cutoff distance (7.88 Å, 20th nearest neighbors), which is mainly due to the enhanced phonon relaxation time. Thus, we believe it is the neglect of *van der Waals* interactions in the work by Jain *et al.* that leads to the different convergence trend of κ vs r_{cutoff}. In this line we also expect that the κ of phosphorene could be largely enhanced by breaking the resonant bonding, such as by applying external tensile strain along the armchair direction. (2) For the calculations of IFCs, different softwares, procedures, and parameters are adopted, which might also have some influence on the results of κ [77]. In another work by Zhu *et al.* [24] based on RTA, the interactions of the third-order IFCs are truncated up to 4.4 Å, i.e., up to the seventh nearest neighbors. Recalling the convergence test of κ as shown in Fig. 4(a), it is no wonder that the κ obtained in their work is quite high.

IV. DISCUSSION AND CONCLUSION

Based on the above results on the phonon anharmonicity and resonant bonding, the low κ of phosphorene associated with the hinge-like structure can be coherently understood. Owing to the weak sp hybridization, the three p electrons are highly delocalized, forming the resonant bonding, while the remaining two s electrons are localized around P atom, forming a lone pair, which leads to a ferroelectriclike lattice instability with electronic polarizability [68–70]. The long-range interactions due to the resonant bonding lead to the low κ by introducing giant phonon anharmonicity and large scattering phase-space volume associated with the soft TO phonon modes [Figs. 1(c)–1(e), 2(c), 2(d), and 3(b)]. Furthermore, due to structural distortion of the hinge-like structure from the original rocksalt structure, the *in-plane* limiting electron configurations are no longer energetically equivalent [69], which weakens the resonant bonding and leads to a significant *in-plane* anisotropy of the lattice dynamics [Figs. 2(a) and 2(b)]. The anisotropic behavior of the *in-plane* bonding feature can be clearly seen from the electron localization function (ELF) [Fig. 3(c)], which is powerful in interpreting the chemical bonding patterns [64,78–80]. Thus the κ of phosphorene exhibits a strong anisotropy. Our three independent *ab initio* methods have unambiguously shown that the κ of phosphorene is anisotropic and intrinsically low, as compared with lots of other 2D materials. Considering the κ of group IV–VI compounds with similar hinge-like structure [64,81], we can conclude that such hinge-like structure generally leads to anisotropic and low κ.

In summary, based on the investigation of electronic structure and lattice dynamics from first principles, we have shown that the giant phonon anharmonicity in phosphorene is associated with the soft TO phonon modes and arises from long-range interactions driven by the resonant bonding. We provide a fundamental microscopic picture to connect the anisotropic and low thermal conductivity of phosphorene to the giant directional phonon anharmonicity and long-range interactions, which are further attributed to the asymmetric resonant orbital occupations of electrons and characteristics of the intrinsic hinge-like structure. The anisotropic and low thermal conductivity of phosphorene is confirmed consistently by employing three independent *ab initio* methods, which is expected to end the confusing huge deviations of the results from previous theoretical studies. We also observe that excluding *van der Waals* interactions breaks the resonant bonding and leads to significantly higher thermal conductivity (mainly due to the enhanced phonon relaxation time), indicating that the *van der Waals* interactions are critical for precisely capturing the nature of interatomic interactions in phosphorene, and should be included to get accurate results when examining the lattice dynamics of phosphorene, which has been neglected in the literature for a long time. The resonant bonding is found to be responsible for the low thermal conductivity of 2D materials with hinge-like structure, despite its originally found in 3D thermoelectric and phase-change materials. Our study highlights the physical origin of the anisotropic and low thermal conductivity of phosphorene and also provides insights into phonon transport from the view of orbital states, which would be of great significance to the design and discovery of novel materials for emerging applications, such as thermal management, thermoelectrics, and phase-change-materials-based rewritable data storage.

ACKNOWLEDGMENTS

G.Q. and M.H. acknowledge Dr. Ankit Jain and Professor Alan J. H. McGaughey (Carnegie Mellon University) for their fruitful discussions. This work is supported by the Deutsche Forschungsgemeinschaft (DFG) (Project No. HU 2269/2-1). The authors acknowledge the computing time granted by the John von Neumann Institute for Computing (NIC) and provided on the supercomputer JURECA at Jülich Supercomputing Centre (JSC) (Project No. JHPC38). The SED calculations were performed with computing resources granted by the Jülich Aachen Research Alliance-High Performance Computing (JARA-HPC) from RWTH Aachen University under Project No. jara0135.

[1] H. Liu, A. T. Neal, Z. Zhu, Z. Luo, X. Xu, D. Tomnek, and P. D. Ye, ACS Nano **8**, 4033 (2014).
[2] L. Li, Y. Yu, G. J. Ye, Q. Ge, X. Ou, H. Wu, D. Feng, X. H. Chen, and Y. Zhang, Nat. Nanotechnol. **9**, 372 (2014).
[3] F. Xia, H. Wang, and Y. Jia, Nat. Commun. **5**, 4458 (2014).
[4] V. Tran, R. Soklaski, Y. Liang, and L. Yang, Phys. Rev. B **89**, 235319 (2014).
[5] A. S. Rodin, A. Carvalho, and A. H. Castro Neto, Phys. Rev. Lett. **112**, 176801 (2014).
[6] J. Qiao, X. Kong, Z.-X. Hu, F. Yang, and W. Ji, Nat. Commun. **5**, 4475 (2014).
[7] H. O. H. Churchill and P. Jarillo-Herrero, Nat. Nanotechnol. **9**, 330 (2014).
[8] Z. Zhu and D. Tománek, Phys. Rev. Lett. **112**, 176802 (2014).
[9] J.-W. Jiang and H. S. Park, Nat. Commun. **5**, 4727 (2014).
[10] Q. Wei and X. Peng, Appl. Phys. Lett. **104**, 251915 (2014).
[11] R. Fei, A. Faghaninia, R. Soklaski, J.-A. Yan, C. Lo, and L. Yang, Nano Lett. **14**, 6393 (2014).
[12] G. Qin, Q.-B. Yan, Z. Qin, S.-Y. Yue, H.-J. Cui, Q.-R. Zheng, and G. Su, Sci. Rep. **4**, 6946 (2014).
[13] T. Low, M. Engel, M. Steiner, and P. Avouris, Phys. Rev. B **90**, 081408 (2014).
[14] S. P. Koenig, R. A. Doganov, H. Schmidt, A. H. Castro Neto, and B. Zyilmaz, Appl. Phys. Lett. **104**, 103106 (2014).
[15] H. Y. Lv, W. J. Lu, D. F. Shao, and Y. P. Sun, Phys. Rev. B **90**, 085433 (2014).
[16] J. Zhu, J.-Y. Chen, H. Park, X. Gu, H. Zhang, S. Karthikeyan, N. Wendel, S. A. Campbell, M. Dawber, X. Du, M. Li, J.-P. Wang, R. Yang, and X. Wang, Adv. Electron. Mater. **2**, 1600040 (2016).
[17] Z. Luo, J. Maassen, Y. Deng, Y. Du, R. P. Garrelts, M. S. Lundstrom, P. D. Ye, and X. Xu, Nat. Commun. **6**, 8572 (2015).
[18] S. Lee, F. Yang, J. Suh, S. Yang, Y. Lee, G. Li, H. Sung Choe, A. Suslu, Y. Chen, C. Ko, J. Park, K. Liu, J. Li, K. Hippalgaonkar, J. J. Urban, S. Tongay, and J. Wu, Nat. Commun. **6**, 8573 (2015).
[19] H. Jang, J. D. Wood, C. R. Ryder, M. C. Hersam, and D. G. Cahill, Adv. Mater. **27**, 8017 (2015).
[20] T.-H. Liu and C.-C. Chang, Nanoscale **7**, 10648 (2015).
[21] Y. Hong, J. Zhang, X. Huang, and X. C. Zeng, Nanoscale **7**, 18716 (2015).
[22] W. Xu, L. Zhu, Y. Cai, G. Zhang, and B. Li, J. Appl. Phys. **117**, 214308 (2015).
[23] Y.-Y. Zhang, Q.-X. Pei, J.-W. Jiang, N. Wei, and Y.-W. Zhang, Nanoscale **8**, 483 (2016).
[24] L. Zhu, G. Zhang, and B. Li, Phys. Rev. B **90**, 214302 (2014).
[25] A. Jain and A. J. H. McGaughey, Sci. Rep. **5**, 8501 (2015).
[26] G. Qin, Q.-B. Yan, Z. Qin, S.-Y. Yue, M. Hu, and G. Su, Phys. Chem. Chem. Phys. **17**, 4854 (2015).
[27] Y. Cai, Q. Ke, G. Zhang, Y. P. Feng, V. B. Shenoy, and Y.-W. Zhang, Adv. Funct. Mater. **25**, 2343 (2015).
[28] G. Kresse and D. Joubert, Phys. Rev. B **59**, 1758 (1999).
[29] G. Kresse and J. Furthmüller, Phys. Rev. B **54**, 11169 (1996).
[30] J. P. Perdew, K. Burke, and M. Ernzerhof, Phys. Rev. Lett. **77**, 3865 (1996).
[31] J. Klimeš, D. R. Bowler, and A. Michaelides, Phys. Rev. B **83**, 195131 (2011).
[32] H. J. Monkhorst and J. D. Pack, Phys. Rev. B **13**, 5188 (1976).
[33] J. Carrete, N. Mingo, and S. Curtarolo, Appl. Phys. Lett. **105**, 101907 (2014).
[34] A. Togo, F. Oba, and I. Tanaka, Phys. Rev. B **78**, 134106 (2008).
[35] K. Esfarjani and H. T. Stokes, Phys. Rev. B **77**, 144112 (2008).
[36] W. Li, L. Lindsay, D. A. Broido, D. A. Stewart, and N. Mingo, Phys. Rev. B **86**, 174307 (2012).
[37] D. A. Broido, M. Malorny, G. Birner, N. Mingo, and D. A. Stewart, Appl. Phys. Lett. **91**, 231922 (2007).
[38] L. Lindsay, W. Li, J. Carrete, N. Mingo, D. A. Broido, and T. L. Reinecke, Phys. Rev. B **89**, 155426 (2014).
[39] A. Ward and D. A. Broido, Phys. Rev. B **81**, 085205 (2010).
[40] A. Ward, D. A. Broido, D. A. Stewart, and G. Deinzer, Phys. Rev. B **80**, 125203 (2009).
[41] M. Omini and A. Sparavigna, Phys. Rev. B **53**, 9064 (1996).
[42] L. Lindsay and D. A. Broido, J. Phys. Condens. Matter **20**, 165209 (2008).
[43] A. Kundu, N. Mingo, D. A. Broido, and D. A. Stewart, Phys. Rev. B **84**, 125426 (2011).
[44] S.-i. Tamura, Phys. Rev. B **27**, 858 (1983).
[45] W. Li, J. Carrete, N. A. Katcho, and N. Mingo, Comput. Phys. Commun. **185**, 1747 (2014).
[46] See Supplemental Material at http://link.aps.org/supplemental/10.1103/PhysRevB.94.165445 for 1. Contribution from each phonon mode to total thermal conductivity; 2. The proportion of N processes in thermal transport of phosphorene; 3. Lorentzian fitting of SED peak; 4. Accumulated thermal conductivity; 5. Vibration direction of phonon modes; 6. Projected electronic band structure; 7. Orbitals; 8. Charge distribution and electron localization function (ELF); 9. Interatomic force constants (IFCs); 10. Charge density perturbation induced by atomic displacement; 11. The effect of interactions cutoff on phonon lifetime and the behavior of size-dependent thermal conductivity; 12. The results calculated with PBE (not including *van der Waals* interactions).
[47] N. de Koker, Phys. Rev. Lett. **103**, 125902 (2009).
[48] J. A. Thomas, J. E. Turney, R. M. Iutzi, C. H. Amon, and A. J. H. McGaughey, Phys. Rev. B **81**, 081411 (2010).
[49] T. Feng, B. Qiu, and X. Ruan, J. Appl. Phys. **117**, 195102 (2015).
[50] J. A. Thomas, J. E. Turney, R. M. Iutzi, C. H. Amon, and A. J. H. McGaughey, Phys. Rev. B **91**, 239905(E) (2015).
[51] X. Zhang, H. Bao, and M. Hu, Nanoscale **7**, 6014 (2015).
[52] S. Stackhouse, L. Stixrude, and B. B. Karki, Phys. Rev. Lett. **104**, 208501 (2010).
[53] S.-Y. Yue, X. Zhang, S. Stackhouse, G. Qin, E. Di Napoli, and M. Hu, Phys. Rev. B **94**, 075149 (2016).
[54] F. Müller-Plathe, J. Chem. Phys. **106**, 6082 (1997).
[55] J. Ziman, *Electrons and Phonons* (Oxford University Press, London, 1961).
[56] G. P. Srivastava, *The Physics of Phonons* (CRC Press, Boca Raton, FL, 1990).
[57] D. L. Nika, E. P. Pokatilov, A. S. Askerov, and A. A. Balandin, Phys. Rev. B **79**, 155413 (2009).
[58] L. Lindsay, D. A. Broido, and N. Mingo, Phys. Rev. B **82**, 115427 (2010).
[59] A. H. Castro Neto, F. Guinea, N. M. R. Peres, K. S. Novoselov, and A. K. Geim, Rev. Mod. Phys. **81**, 109 (2009).
[60] X. Zhang, H. Xie, M. Hu, H. Bao, S. Yue, G. Qin, and G. Su, Phys. Rev. B **89**, 054310 (2014).
[61] H. Xie, M. Hu, and H. Bao, Appl. Phys. Lett. **104**, 131906 (2014).
[62] H. Xie, T. Ouyang, E. Germaneau, G. Qin, M. Hu, and H. Bao, Phys. Rev. B **93**, 075404 (2016).

[63] R. Fei and L. Yang, Nano Lett. **14**, 2884 (2014).
[64] G. Qin, Z. Qin, W.-Z. Fang, L.-C. Zhang, S.-Y. Yue, Q.-B. Yan, M. Hu, and G. Su, Nanoscale **8**, 11306 (2016).
[65] O. Delaire, J. Ma, K. Marty, A. F. May, M. A. McGuire, M.-H. Du, D. J. Singh, A. Podlesnyak, G. Ehlers, M. D. Lumsden, and B. C. Sales, Nat. Mater. **10**, 614 (2011).
[66] W. G. Zeier, A. Zevalkink, Z. M. Gibbs, G. Hautier, M. G. Kanatzidis, and G. J. Snyder, Angew. Chem. Int. Ed. Engl. **55**, 6826 (2016).
[67] L.-D. Zhao, C. Chang, G. Tan, and M. G. Kanatzidis, Energy Environ. Sci. **9**, 3044 (2016).
[68] S. Lee, K. Esfarjani, T. Luo, J. Zhou, Z. Tian, and G. Chen, Nat. Commun. **5**, 3525 (2014).
[69] K. Shportko, S. Kremers, M. Woda, D. Lencer, J. Robertson, and M. Wuttig, Nat. Mater. **7**, 653 (2008).
[70] C. W. Li, J. Hong, A. F. May, D. Bansal, S. Chi, T. Hong, G. Ehlers, and O. Delaire, Nat. Phys. **11**, 1063 (2015).
[71] J. Larkin, J. Turney, A. Massicotte, C. Amon, and A. McGaughey, J. Comput. Theor. Nanosci. **11**, 249 (2014).
[72] N. Bonini, J. Garg, and N. Marzari, Nano Lett. **12**, 2673 (2012).
[73] T. Feng, B. Qiu, and X. Ruan, Phys. Rev. B **92**, 235206 (2015).
[74] Z.-X. Hu, X. Kong, J. Qiao, B. Normand, and W. Ji, Nanoscale **8**, 2740 (2016).
[75] A. A. Balandin, Nat. Mater. **10**, 569 (2011).
[76] X. Gu, B. Li, and R. Yang, J. Appl. Phys. **119**, 085106 (2016).
[77] A. Jain and A. J. McGaughey, Comput. Mater. Sci. **110**, 115 (2015).
[78] A. Savin, R. Nesper, S. Wengert, and T. F. Fssler, Angew. Chem. Int. Ed. Engl. **36**, 1808 (1997).
[79] S. N. Steinmann, Y. Mo, and C. Corminboeuf, Phys. Chem. Chem. Phys. **13**, 20584 (2011).
[80] X. Wu, V. Varshney, J. Lee, T. Zhang, J. L. Wohlwend, A. K. Roy, and T. Luo, Nano Lett. **16**, 3925 (2016).
[81] L.-C. Zhang, G. Qin, W.-Z. Fang, H.-J. Cui, Q.-R. Zheng, Q.-B. Yan, and G. Su, Sci. Rep. **6**, 19830 (2016).